## Title
Shear band patterning and post-critical behavior in AISI 4340 steel with different microstructure



**Authors**
Navarro, Pedro Franco
Chiu, Po-Hsun
Higgins, Andrew
et al.

**Publication Date**
2018-02-01

**DOI**
10.1016/j.ijimpeng.2017.10.011

Peer reviewed

# Shear band patterning and post-critical behavior in AISI 4340 steel with different microstructure

Pedro Franco Navarro[*], Po-Hsun Chiu[**], Andrew Higgins[***], Matthew Serge[***], David J. Benson[****], and Vitali F. Nesterenko[*,**]

[*]Department of Mechanical and Aerospace Engineering, University of California, San Diego, P.O. Box 0411, 9500 Gilman Drive, La Jolla, CA, 92093,

[**]Materials Science Graduate Program, University of California, San Diego, P.O. Box 0418, 9500 Gilman Drive, La Jolla, CA, 92093,

[***]Department of Mechanical Engineering, McGill University, Quebec, Canada H3A 0C3,

[****]Department of Structural Engineering, University of California, San Diego, P.O. Box 0418, 9500 Gilman Drive, La Jolla, CA, 92093,

Abstract: We explore the role of the microstructure of AISI 4340 steel with different values of microhardness (as-received and hardened) on shear band nucleation and post-critical behavior with well-developed pattern of shear bands. Critical and post-critical behavior was investigated with the help of the explosively-driven Thick-Walled Cylinder technique, which allowed comparative study of the material deformation at similar strain rates and final strains. It was observed that the collapsed as-received AISI 4340 samples were resilient to shear localization and propagation and mainly preserved its cylindrical geometry at the investigated small and larger global strains. The hardened specimens at the similar final global strains exhibited dramatically different behavior. At small strains, some well-developed shear bands were observed.  Larger global strains were accommodated mostly by growth of the initially generated shear bands, resulting in the complete loss of cylindrical symmetry. Numerical simulations reproduced the main features observed in the experiments and the dramatic difference in behavior of as-received and hardened AISI 4340 steel. It is shown that the initial number of defects introduced in calculations as well as the material constants used for the material model have a direct effect on the pattern of shear bands.

## 1. Introduction

Shear localization is an important deformation and failure mechanism for materials that have been subjected to high strain rate deformation, e.g., high-velocity impact and penetration, in high-speed metal cutting, and during collapse of cylindrical cavities [1-5]. Shear bands have been extensively studied starting with the paper by Zener and Hollomon [6], which introduced adiabatic shear bands (ASBs). It was recently brought to light [7] that Tarnavskii in 1928 [8] and Davidenkov and Mirolubov in 1935 [9] gathered the first evidence of ASB in steels.

In this paper, we focus on the pattern of multiple shear bands in AISI 4340 steel (as received vs. hardened) using the Thick-Walled Cylinder (TWC) method. This post-critical behavior is important in many applications, it being responsible for the material's ability to dissipate the mechanical energy due to viscoplastic deformation. The explosively-driven method was proposed by Nesterenko et al. [4, 10-16] to investigate spontaneous shear instability, patterns of shear bands in solid and granular materials, and buckling of laminates (inert and reactive). It also was used by other researchers [17,18] and later modifications of this method using electromagnetic drive [19-23], Hopkinson bar [24], and gas gun [25].

Analytical approaches to describe the thickness and spacing of adiabatic shear bands have been developed starting with the paper by Grady and Kipp [26] and detailed explanations can be found in [2, 27-29]. Nevertheless, these models describe only qualitative results, and fail to recapture both length and spacing observed in experiments. Although results are in the same order of magnitude, they are off by a factor of 3-4 [21].

Numerical calculations were used to study formation and evolution of ASB and their emerging self-organized pattern in the geometry corresponding to the TWC test in different materials such as Cu, Ti, and AISI 304L in [19-21, 30-33]. The difference in these approaches lies in the failure criteria that give a positive feedback mechanism for the strain localization. These authors invoked energy or strain criteria [21-23] weakening the material and resulting in nucleation of a shear band. In [22] authors connected rapid development of localization in Ti6Al4V to dynamic recrystallization and delay in shear localization in CP-Titanium and in MgAM50 to a significant twinning absent in Ti6Al4V. The highest number of shear bands in SS304L is attributed to both twinning and martensitic transformation being active.

In [31], the authors emphasized a need of defects to nucleate shear bands in their numerical approach. The interplay between the number of shear bands and its propagation is directly related to the initial defect distribution. In [32,33], the authors reproduced the nucleation of strain localization and generated a pattern of shear bands without the introduction of any defects in the materials or the meshes. The authors employed a temperature perturbation that helped break the homogeneity and cause localization.

AISI 4340 steel has unique properties and applications related to high strain rate deformation of penetrators and armor plates. Extensive research has been conducted to understand its response to shear band nucleation and propagation [34-36].

The failure mechanism of AD95 ceramic/4340 steel composite armor during the impact of a tungsten projectile at velocity about 820 m/s was studied in [34]. Different failure modes corresponding to various target configurations were observed.

In [35], authors study penetration of ogive-nose steel projectiles made from 4340 ($R_c$ 45) on concrete targets. Projectiles had a speed of either 400 m/s or 1200 m/s. In experiments, it was shown that penetration depth increased with speed, but once data was normalized by length scale determined by the model of the authors, the data collapsed on a single curve.

Authors of [36] conduct a study of penetration in semi-infinite 4340 targets by tungsten-alloy projectiles at 1500 m/s. In this study, experimental results are compared to numerical simulations that use the Johnson-Cook material model; this is analogous to what is done in this work. Authors found that when the ratio of target diameter to projectile diameter is below 20 target resistances rapidly decreases. With the use of simulations, authors found out that penetration increases when the region of plastic flow is close to the radial boundary of the target.

Numerous studies have focused on understanding the formation of multiple shear bands in the machining process of this steel at various cutting speeds, ranging from 100 m/min to 3000 m/min [37-39]. The main interest of understanding shear band formation in the cutting process is related to the surface finish, which could greatly affect the performance of the finished part. It was found that, in general, cutting speeds as well as characteristics of the steel, like hardness, dictate chip formation. Specifically, in [37], the authors conducted a computational study using the Johnson-Cook material model with damage to simulate chip morphology. This approach is similar to what we present in the present paper.

The single shear band formation in AISI 4340 steel due to high velocity impact was investigated in papers [40-44]. Different techniques, like Hopkinson bar tests or expanding cylinder tests, are used to produce strain rates in the range $10^2 – 10^5$ $s^{-1}$, without the control of the total global strains. It was concluded that initiation sites for the formation of shear bands occurred at the interface of the carbide inclusions and the matrix. In [42], the authors used numerical calculations to reproduce adiabatic shear observed in experiments using a Hopkinson bar. Their simple criteria to predict the onset of instabilities is based on a maximum shear stress under a minimum critical shear strain rate. It proved to be capable of predicting the start of the instability, but not its evolution on the post critical stage.

The previous research has been focused on understanding the development of single shear bands through experiments and numerical simulations and understanding the mechanism of their formation and propagation in AISI 4340 steel. At the same time, in many applications a pattern of shear bands is generated, which determined the performance of the devices or quality of the machining. In this paper, we generated a pattern of shear bands in a plane strain controlled environment using the Thick-Walled Cylinder (TWC) method to understand the interplay and propagation of multiple shear bands in AISI 4340 steel under a controlled global strain. Two types of AISI 4340 steel with different initial microstructure were explosively driven with identical conditions of the dynamic deformation. These specimens had different mechanical properties (e.g., strength and ductility) due to a heat treatment described below. They had similar thermophysical properties (e.g., density, heat capacity and thermal conductivity), which favorably restricts the number of variable properties of the samples. Numerical simulations were conducted to understand the influence of the material mechanical properties on the generated pattern of self-organized shear bands. A different distribution of defects was introduced in the material to better replicate the experimental results.

## 2. Experimental procedure and results

Cylindrical samples were machined from the cold-drawn AISI 4340 steel rod processed by air melt (McMaster-Carr) and had an initial outer diameter (O.D.) of 17.02 mm, inner diameter (I.D.) of 12.07mm, and height of 20mm. They were used as inserts in the TWC method and were dynamically collapsed under plane strain conditions. The details of the method can be found in [14]. The explosive driver was a gelled nitromethane (96% nitromethane, 4% PMMA) diluted 5% by mass with glass microballoons. The same driver was used in [15] and [16] and allowed for the fine tuning of the explosive loading.

As-received AISI 4340 steel has proeutectoid ferrite and pearlite (alternating layers of ferrite and cementite). Some specimens were austenized at 845 °C, oil quenched and tempered at 205 °C for two hours to increase its hardness. During the first austenizing stage of hardening, the steel was completely transformed to austenite. In the next stage, during fast oil-quenching, the steel was transformed to a martensite microstructure resulting in a very hard and brittle material. To enhance its ductility and toughness, tempering was carried out at 205  C to produce a tempered martensite structure, which consisted of thin precipitated platelet and spherical carbides immersed in the tempered martensite lath matrix [45, 46]. The microstructure of as-received and hardened AISI 4340 steel are presented in Fig. 1.

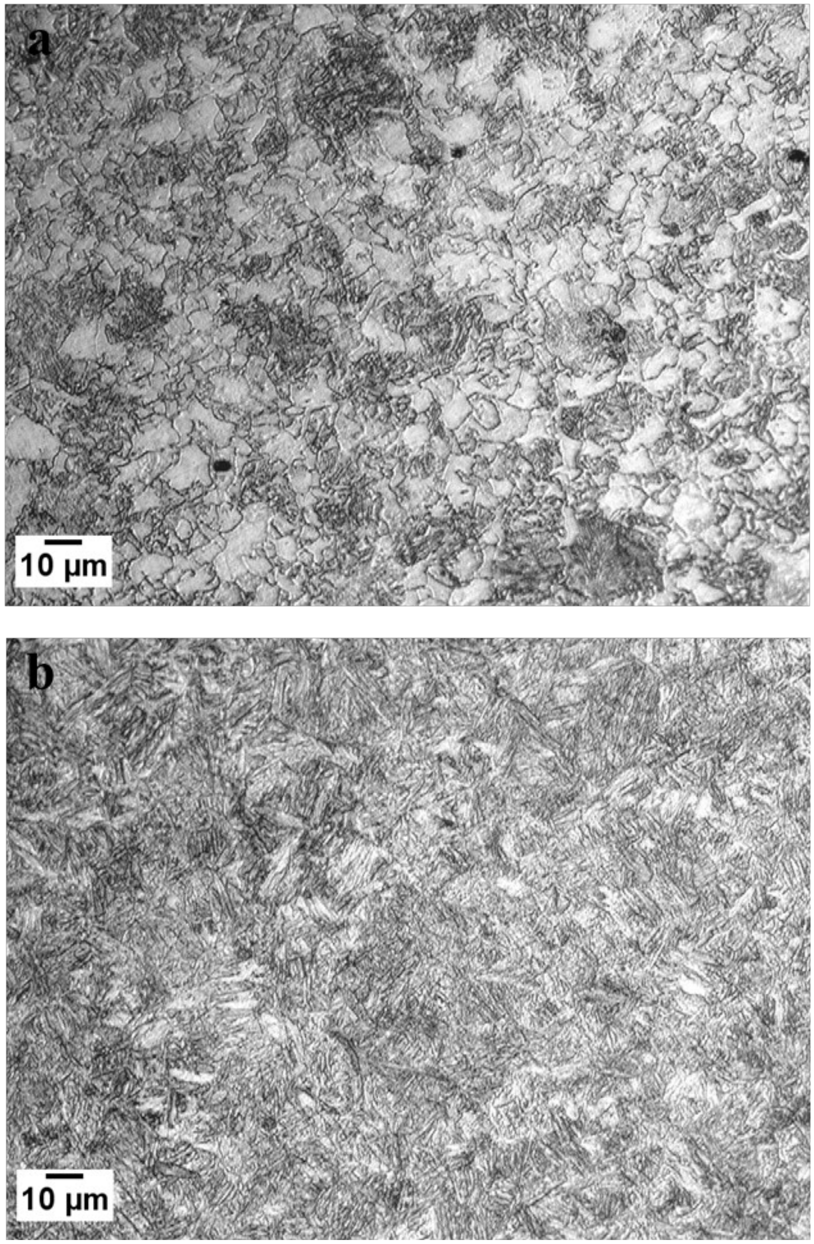


**Figure 1.** The microstructure of as-received AISI 4340 (ferrite is white and pearlite is dark gray) - (a) and hardened AISI 4340 steel with martensite microstructure- (b).

The properties of the investigated steels are presented in Table 1. The microhardness of as-received and hardened AISI 4340 steel before testing was measured according to ASTM E92 Standard. A LECO Model M400-H1 hardness tester with a diamond-shaped indenter was used and a load of 500gf was applied on the samples for 15 seconds. After the heat treatment, the microhardness of AISI 4340 steel increased significantly from 2789±23 MPa to 5420±45 MPa. The ultimate tensile strength ($\sigma_u$), 0.2% yield strength ($\sigma_{0.2}$), elongation ($\delta$), true strain at fracture ($\delta_f$), thermal conductivity at 100 °C ($k$), specific heat ($S$), plane-strain fracture toughness ($K_{IC}$) are taken from [47], where corresponding properties of as-received and hardened AISI 4340 steel were reported.

**Table 1.** Mechanical properties of as-received and hardened AISI 4340 steels [47]

| Sample Type | $\sigma_u$ [47] (MPa) | $\sigma_{0.2}$ [47] (MPa) | $\delta$ [47] (%) | $\delta_f$ [47] (%) | $k$ [47] (W/m·K) | $S$ [47] (J/kg·K) | $K_{IC}$ [47] (MPa√m) | Microhardness (MPa) |
|---|---|---|---|---|---|---|---|---|
| as-received | 745 | 470 | 22 | 21 | 42.7 | 475 | 110 | 2789±23 |
| hardened | 1980 | 1860 | 10 | 10 | 42.7 | 475 | 48 | 5420±45 |

The TWC experiments were conducted on the steel specimens with two different wall thicknesses of copper stopper tubes: 1 and 0.5 mm. These stopper tubes were collapsed into rods with different diameters; tubes with 1 mm wall thickness resulted in a "small global strain" and tubes with 0.5 mm wall thickness produced a "large global strain" in the samples. Strains were calculated assuming the global cylindrical symmetry of the deformation and using the initial radii ($r_0$) and final radii ($r_f$) of the corresponding points per equation (1), and the results are shown in Table 2,

$$\varepsilon_{eff} = \frac{2}{\sqrt{3}} \ln\left(\frac{r_0}{r_f}\right) \tag{1}$$

**Table 2** Final diameters of the AISI 4340 samples, which have identical initial O.D. (17.02 mm) and I.D. (12.07mm), and the corresponding effective strains ($\varepsilon_{eff}$).

| | Final O.D. (mm) | Final I.D. (mm) | $\varepsilon_{eff}$ (on the inner surface) | $\varepsilon_{eff}$ (on the outer surface) |
|---|---|---|---|---|
| as-received (small ε) | 14.22 | 7.63 | 0.53, start of shear localization | 0.21 |
| as-received (large ε) | 13.44 | 6.05* | 0.80, slight grow or shear localization | 0.27 |
| hardened (small ε) | 14.11 | 7.42* | 0.56, developed shear bands pattern | 0.22 |
| hardened (large ε) | 13.36 | 5.86* | 0.83, fragmentation of the sample | 0.28 |

* Estimated values used initial and final radii of copper stopper tube based on mass conservation.

Images of the samples after tests are presented on Figs. 2-7. Figure 2 presents the case of as-received AISI 4340 samples corresponding to small (Fig. 2(a)) and large (Fig. 2(b)) global strains. It is clear that the global cylindrical symmetry of the specimens was preserved and thus global strains in the inner surfaces of the collapsed samples are computed: $\varepsilon_{eff} = 0.53$, for the case of small global strain, and $\varepsilon_{eff} = 0.80$ for the large global strain. The small-diameter hole in the center of the collapsed copper stopper corresponds to the axial jetting removing only small amounts of the copper, which was verified by comparison of the final diameter of the copper stopper tube in experiments and based on mass conservation.

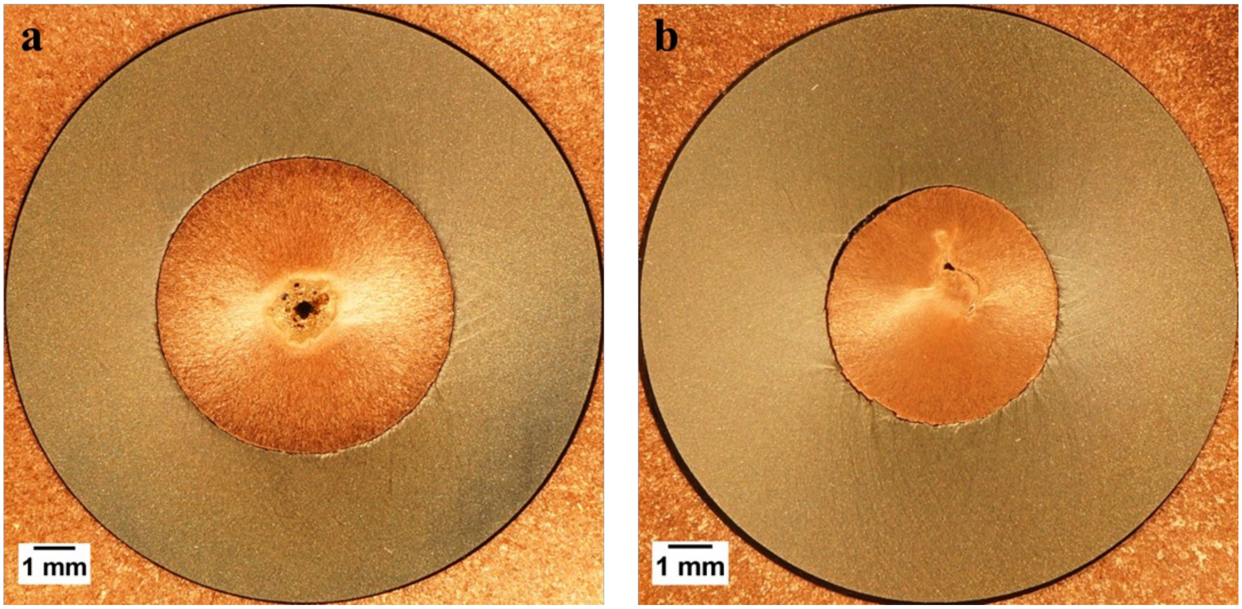


**Figure 2.** Pictures of the collapsed AISI 4340 samples (as-received) at a different strain in the inner surface: (a) strain 0.53, initial wall thickness of the copper stopper tube 1 mm and (b) strain 0.80, initial wall thickness of the copper stopper tube 0.5 mm.

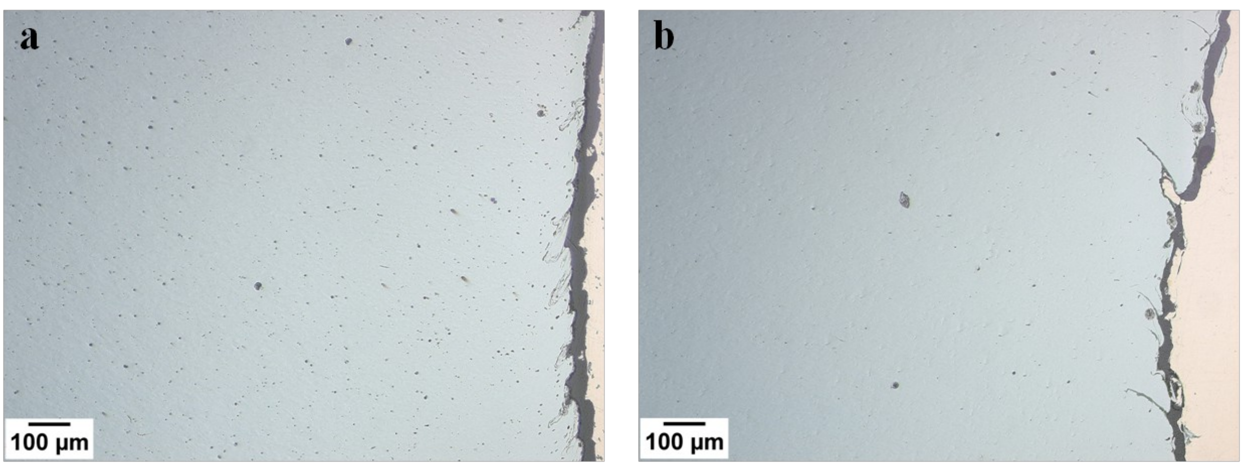


**Figure 3.** Pattern of nucleating shear bands in the vicinity of the contact with copper stopper tube in collapsed AISI 4340 (as-received) samples at different values of strain in the inner surface: (a) strain 0.53, initial wall thickness of the copper stopper tube 1 mm and (b) strain 0.80, initial wall thickness of the copper stopper tube 0.5 mm.

A pattern of nucleated shear bands can be observed in the case of small global strain (Fig. 2(a) and 3(a)). In the case of larger global strain (Fig. 2(b) and 3(b)), the pattern of longer shear bands has developed closer to the inner surface of the sample. Thus, a reasonable estimate of the nucleation strain for the formation of shear band patterns in as-received AISI 4340 steel is $\varepsilon_{eff}$ = 0.53. This value is close the strain value of 0.5, sufficient to induce a shear instability in pearlitic AISI 4340 steel in dynamic punch-impact tests at an average strain rate of 18,000 $s^{-1}$ [48]. It seems that the spacing along the inner radius between nucleated shear bands is smaller in the sample with smaller global strain (about 200µm, Fig. 3(a)) compared to the spacing between longer shear bands (with lengths >100µm) in the sample with larger global strain (about 300µm, Fig. 3(b)). This behavior is similar to that observed in AISI 304 steel, where the development of some shear bands arrests the growth of others due to unloading [13]. In both collapsed samples, no catastrophic failure occurred.

The dramatically different behavior of the hardened AISI 4340 steel is presented in Fig. 4.

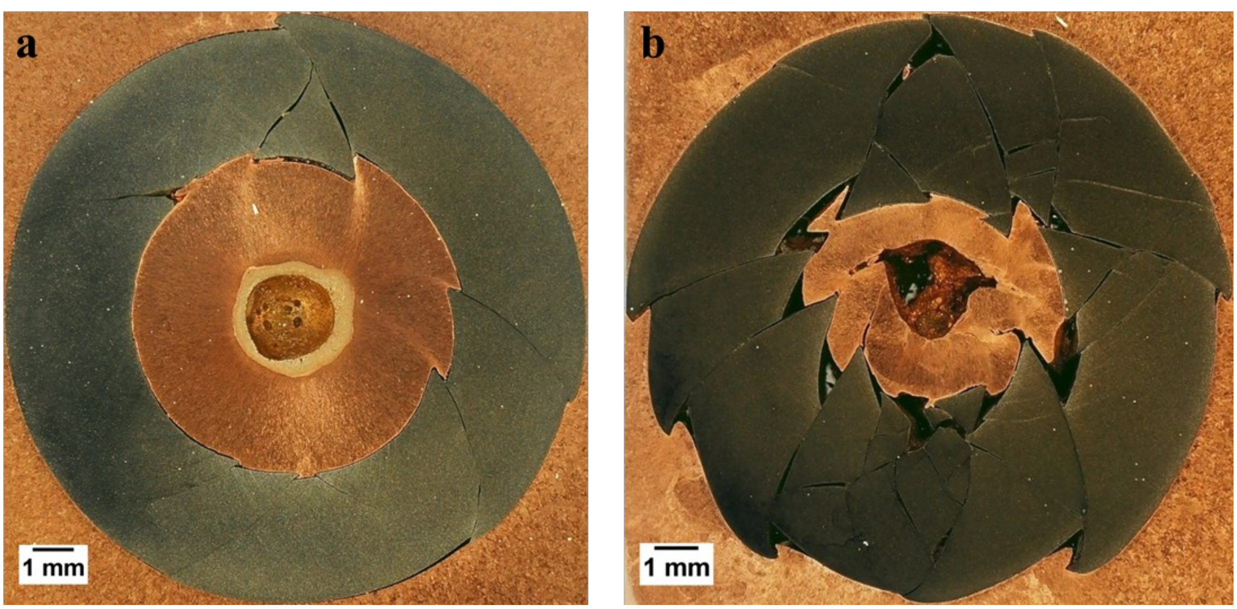

**Figure 4.** Pictures of the collapsed AISI 4340 samples (hardened) at a different strain in the inner surface: (a) strain 0.56, initial wall thickness of a copper stopper tube 1 mm and (b) collapse steel sample corresponding to the initial wall thickness of a copper stopper tube 0.5 mm.

At both tests with different wall thickness of copper stopper tubes (used to generate different global strains), well-developed shear bands are evident. From Fig. 4 it is possible to conclude that the difference in microstructure and change of the mechanical properties resulted in the creation and propagation of shear bands throughout the entire steel sample. As a result, the symmetry of the collapsed steel samples has been lost and catastrophic failure of the steel specimen happened. Still, the collapsed sample at small strains in Fig. 4 (a) mostly preserved a cylindrical symmetry and thus Eq. 1 can be used to estimate the global strains in the inner surface of the sample as $\varepsilon_{eff} = 0.56$, which can be considered as being close to the nucleation strain for the formation of shear bands in hardened AISI 4340. But comparison between Figs. 2a, 3a, and 4a demonstrate that critical strain for shear band propagation is smaller in hardened AISI 4340.

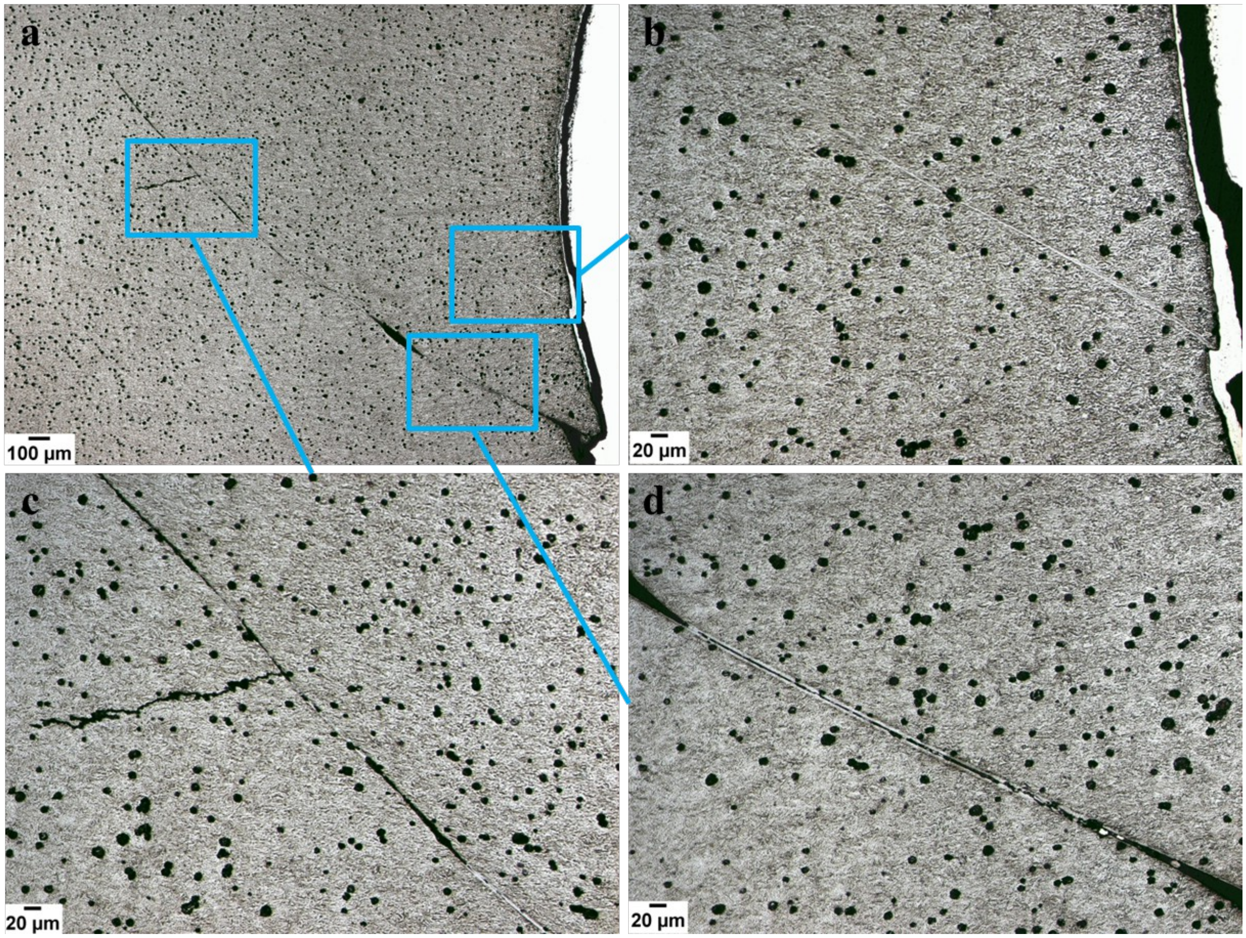


**Figure 5.** Microstructures of the collapsed AISI 4340 (hardened) sample with strain 0.56 in the inner surface (initial wall thickness of the stopper copper tube 1 mm). Just nucleated and well-developed shear bands are presented in (a); a white-etched nucleated shear band without microcrack is shown in (b). Bifurcated shear band developed probably due to the weak interface between inclusions and the matrix, is shown in (c). The coalescence of microcracks into macrocrack in a white-etching band is shown in (d).

Microstructures of the collapsed AISI 4340 (hardened) samples are shown in Figs 5 and 6. White-etching or transformed bands were revealed by etching with 2% nital. A just nucleated shear band without microcrack and a well-developed, partially cracked and bifurcated shear band are shown in Fig. 5 (a). A larger magnification of the former is presented in Fig. 5(b) and segments of developed shear bands are shown in Figs. 5(c) and (d). The bifurcation of the shear band presented in Fig. 5(c) seems due to its interaction with the weak interface between the inclusion and the surrounding matrix. Several microcracks inside a white-etching band were observed in Fig. 5(d), which can be precursors for macrocracks. We can also observe the microcrack present between segments of white-etching band (Fig. 6), which was probably originated from an initially transformed segment of shear band.

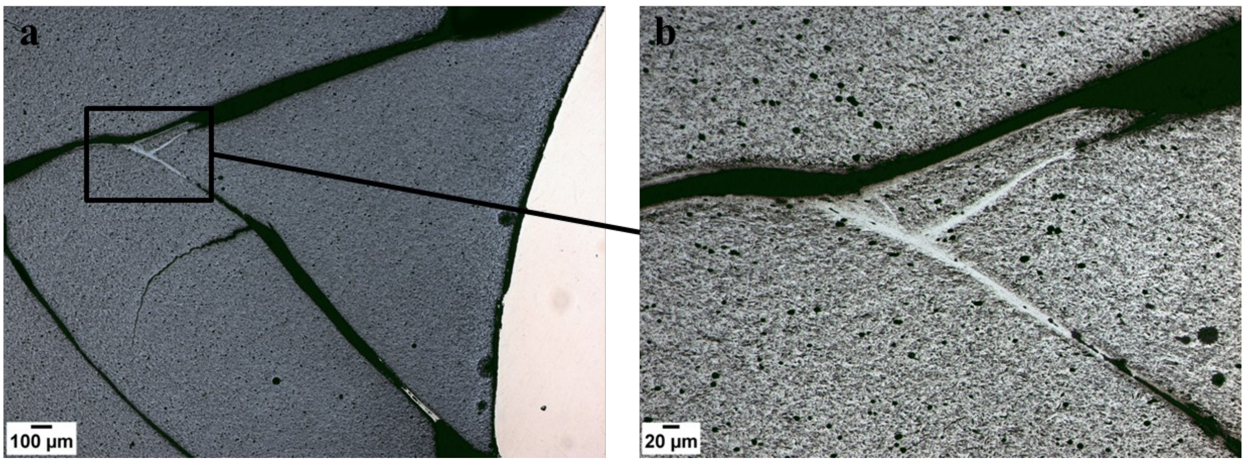


**Figure 6.** Microstructures of bifurcated shear band split into two transformed shear bands and later into crack, at different magnifications in the collapsed hardened AISI 4340 sample at strain in the inner surface 0.83 (initial wall thickness of the copper stopper tube 0.5 mm). Sample was etched with 2% nital.

In tests with as-received AISI 4340 only deformed shear bands were observed (Fig. 7) and in hardened AISI 4340 steel showed the segments of transformed (white-etching) bands presented in Fig. 5 and 6, corresponding to different global strains in tests with the wall thickness of the copper stopper tube equal to 1 and 0.5 mm. A controlled heating and cooling process of 4340 steel was used to change the microstructure and obtain higher strength and lower ductility. During this treatment the martensite phase transformation was completed before TWC tests. It is possible that inside well developed shear bands initial martensite phase was transformed to austenite due to localized heating and returned back to martensite with much smaller grain sizes than in initial material due to subsequent fast quenching. This resulted in a white transformed shear bands with different appearance than the surrounding martensite matrix.

The dependence of the types of shear bands on steel microstructure was observed in [49], where white-etching shear bands were only found in quenched and quenched-and-tempered steel.

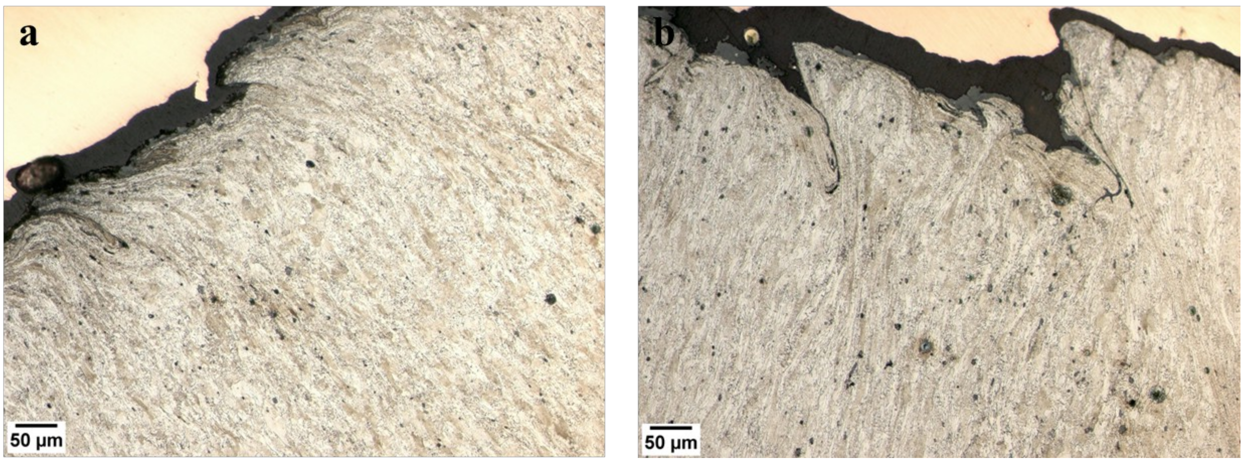


**Figure 7**. Shear bands in the collapsed AISI 4340 (as-received) sample etched with 2% natal at different values of strain in the inner surface: (a) strain 0.53, initial wall thickness of the copper stopper tube 1 mm and (b) strain 0.80, initial wall thickness of the copper stopper tube 0.5 mm.

We can observe microcracking inside shear band in the area adjacent to the copper stopper tube (Fig. 7), which probably initiated at the interface between matrix and inclusions, extending into deformed shear bands.

The microstructure of the shear bands in Fig. 5 suggests that the propagation mechanism of shear bands in the hardened AISI 4340 sample is related to the interfacial microcracking between the inclusions and matrix similar to [50, 51] (the authors of [51] mentioned that voids are nucleated at the interface of large MnS inclusions and matrix, which then nucleated a sheet of voids on the much smaller cementite particles between the large voids formed at the MnS particles). Coalescence of voids and microcracks at the interfaces between the inclusions and matrix in the shear band can result in void sheet formation [50, 51]. A similar mechanism is probably responsible for the propagation of shear bands and their bifurcation as well as a zig zag shape of bifurcated shear band in hardened AISI 4340 steel (Fig. 5(c)).

The authors of [52] emphasized that the presence of hard particles or secondary precipitates in the ferrite matrix of steel facilitates the occurrence of ASBs. In comparison to pearlitic steels of similar hardness, martensitic steels have a greater tendency to form localized shear bands [53]. Different mechanical properties, owed to different microstructures (pearlite or martensite, concentration and shape of cementite inclusion) of as-received and hardened AISI 4340, are responsible for their different behavior in our experiments.

We can speculate that the difference in post-critical behavior of as-received and hardened AISI 4340 steel results from the difference in dissipation of mechanical energy in the bulk of the samples. In the latter case, global strains are accommodated mostly by the pattern of shear bands with low shear strength inside the bands resulting in reduced dissipation. This may explain a larger area of the central melt in the collapsed copper stopper tube caused by the concentration of kinetic energy of collapsing tube and axial micro jetting (compare Fig. 2 and Fig. 4).

It is interesting that spontaneous shear bands developed in hardened AISI 4340 created the forced shear bands in the copper stopper tube, evident in Fig. 4(b). In general, copper is very resistant to spontaneous shear localization due to its low strength and high heat conductivity.

## 3. Numerical Calculations

Numerical calculations were performed using LS-DYNA with the Johnson-Cook [54] material model coupled with the Mie-Grüneisen equation of state. In the Johnson-Cook material model, the flow stress is given by:

$$\sigma_y=\left(A+B\acute{\epsilon}^{p\,n}\right)\left(1+c\ln\dot{\epsilon}^{*}\right)\left(1-T^{*m}\right) \quad (2)$$

In this model, $A$, $B$, $c$, $n$, and $m$ are model constants, $\acute{\epsilon}^{p}$ is the effective plastic strain, and $\dot{\epsilon}^{*}$ is the normalized effective total strain-rate. The action of the explosive was modeled using a pressure boundary condition similar to [21,30] that collapses the central cavity in about 10 μs. To capture damage, we used the approach presented in [54]:

$$D=\sum\frac{\Delta\epsilon}{\epsilon^{f}}, \quad (3)$$

where $\Delta\epsilon$ is the increment of equivalent plastic strain during an integration cycle and $\epsilon^{f}$ is the equivalent strain at fracture, when $D$ =1, fracture occurs and the element is eroded. The general expression for the strain at fracture is given by:

$$\epsilon^f = [D_1 + D_2 \exp D_3 \sigma^{*}][1 + D_4 \ln \dot{\epsilon}^{*}][1 + D_5 T^{*}] \quad , \tag{4}$$

with $\sigma^{*} = P/\sigma_{eff}$, i.e., pressure divided by the effective stress, and $D_1 - D_5$ are experimentally determined parameters [54].

The geometry used in the numerical calculations is similar to the experimental set up and it is shown in Fig. 8(a). As mentioned before, we use a pressure boundary condition (Fig. 8(b)) to replace the explosive used in the experiments; a separate calculation with the Jones-Wilkins-Lee equation of state for the explosive was made to assure a good reproduction of the experimental conditions. The process of the collapse of the steel sample was driven to the same outer radius of the samples as observed in the experiments. The mesh size used in the numerical calculations of the collapse of the AISI 4340 steel sample (shown in red in Fig. 8(a)) was about 10 μm, for the copper stopper (inner blue circle), and the mesh size was about 15-20 μm and for the copper driver (outer blue circle) about 50 μm. This mesh size was selected to approximate correctly the characteristic size of shear bands observed in the experiments. All the numerical calculations were executed in plane strain conditions that correspond to the experimental conditions.

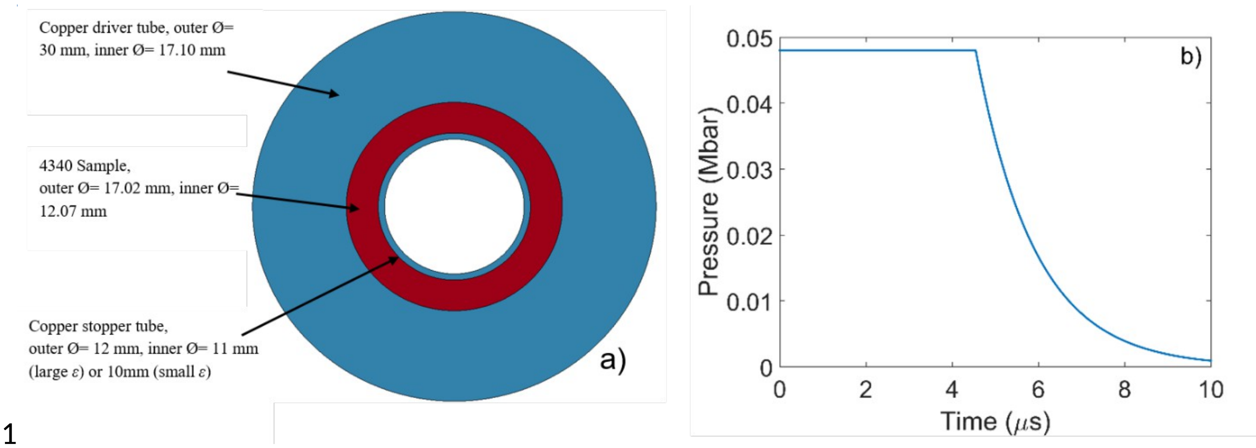


**Figure 8.** (a) Geometry of the Thick-Walled Cylinder method (b) Pressure dependence on time corresponding to the boundary conditions used in numerical calculations.

The mechanical properties of AISI 4340 steel and copper were taken from [54,55], for both cases, the reference strain rate is 1 $s^{-1}$. It is important to remark that the constants used in the Johnson-Cook model are selected to fit experimental stress-strain curves at different strain rates and temperatures.

**Table 3.** Material parameters for Johnson-Cook material model [54,55].

| | *A* [MPa] | *B* [MPa] | *n* | *C* | *m* |
|---|---|---|---|---|---|
| AISI 4340 | 792 | 510 | 0.26 | $1.4x10^{-2}$ | 1.03 |
| 4340 Hardened | 2100 | 1750 | 0.65 | $2.8x10^{-3}$ | 0.75 |
| Copper | 90 | 292 | 0.31 | $2.5x10^{-2}$ | 1.09 |
| | Density [$kg/m^3$] | Elastic Modulus [GPa] | Poisson's Ratio | Specific Heat [J/kgK] | Melting Temp [K] |
| AISI 4340 | 7830 | 207 | 0.29 | 477 | 1793 |
| 4340 Hardened | 7830 | 207 | 0.29 | 477 | 1793 |
| Copper | 8960 | 124 | 0.34 | 383 | 1356 |
| | D1 | D2 | D3 | D4 | D5 |
| AISI 4340 | 0.05 | 3.44 | -2.12 | 0.002 | 0.61 |
| 4340 Hardened | 0.05 | 3.44 | -2.12 | 0.002 | 0.61 |
| Copper | 0.54 | 4.89 | -3.03 | 0.014 | 1.12 |

At first, simulations were conducted with nominal material properties corresponding to AISI 4340 and no defects were introduced. The result presented in Fig. 9 corresponds to a uniform collapse of the steel specimen without the initiation of shear localization, even though the model had softening mechanisms related to the thermal softening and damage accumulation. The same uniform collapse was observed for hardened AISI 4340.

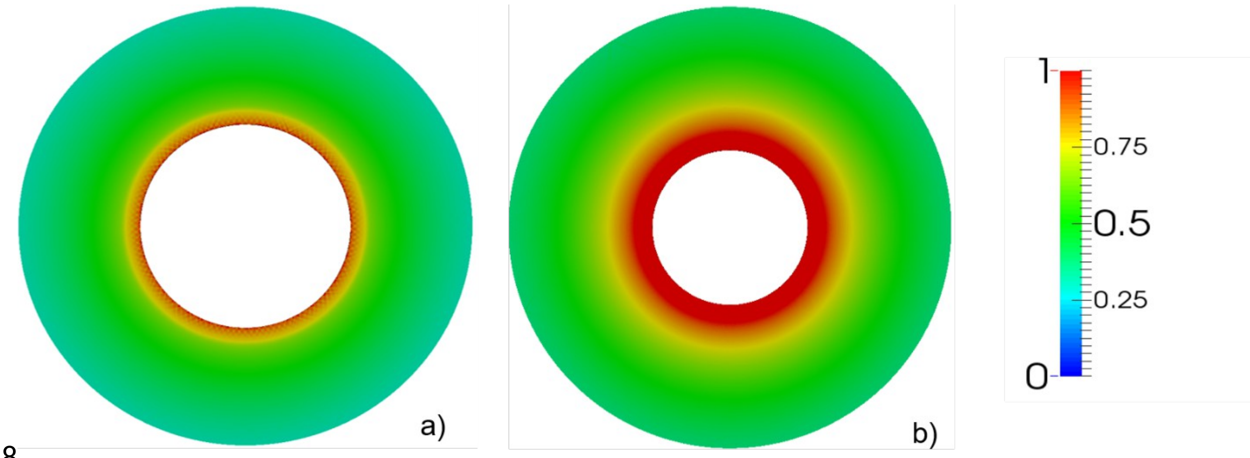


**Figure 9**. Collapsed AISI 4340 steel cylinder at (a) small global strain (1 mm wall thickness copper stopper) and (b) large global strain (0.5 mm wall thickness copper stopper). The colors on right correspond to different level of effective plastic strains.

Figure 9 shows that the inner surface was naturally subjected to the highest level of strain with the width of the heavily deformed zone increasing with decrease of the final diameter.

The TWC test was designed in a way wherein the massive copper driver tube collapses the samples having different strengths with a similar strain rate. To illustrate, this point we a conducted numerical calculation of the collapse process with different strength of the samples. Figure 10 shows the total velocity of the inner surface of the collapsing samples for AISI 4340 and for hardened AISI 4340.

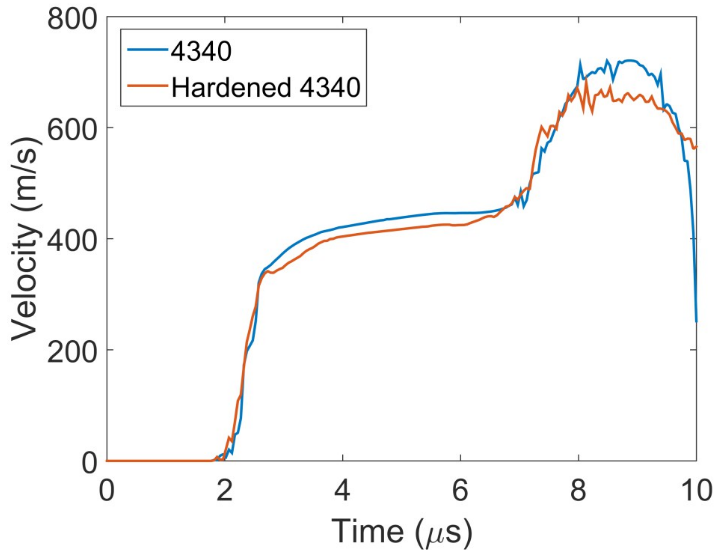


**Figure 10.** Total velocity of inner surface in numerical simulations of steel specimen on Thick-Walled Cylinder experiment of AISI 4340 (blue line) and heat treated 4340 (red line)

It is clear that the dynamics of collapse of these two samples with dramatically different strength are practically identical in the geometry of the TWC test.

*3.1 Influence of the Number of Defects on Shear localization and Post-Critical Behavior of AISI 4340*

The results of the numerical calculations demonstrate that high strain plastic flow, even with a softening mechanism incorporated, does not result in shear instability (Fig. 9) contrary to the experimental observations (Figs. 3-7). It should be mentioned that steel samples do have a significant number of inclusions (Figs. 5-7) whose interfaces with the surrounding matrix are potential sites for microcracking serving as a softening mechanism essential for shear localization [50,51]. This mechanism should be taken into account to explain the observed phenomena of shear instability and the pattern of shear bands.

It has been shown that the “defects” introduced in the numerical calculations have a direct effect on the number of nucleated and evolved shear bands in the steel specimen corresponding to the TWC experimental set up [31]. The authors of this paper found that smaller scatter of material properties effectively increases the number of generated shear bands, but their length decreased. Thus, the interplay of material imperfections and instabilities plays a critical role in the final pattern of shear bands.

To explore the role of initial defects on nucleation and propagation of shear bands, we performed calculations corresponding to collapsed AISI 4340 samples with nominal properties (Table 3) in the majority of mesh elements and variable percentages (5%, 2.5%, 1.5%, and 0.5%) of mesh elements that have a different initial yield strength scaled by the nominal yield strength:

$$\sigma_{y_{Scaled}} = \sigma_y \cdot P \quad . \tag{5}$$

The “defects” are randomly distributed through the steel specimen and the scaling factor $P$ follows the following normal distribution $N(0.1, 0.0025)$, the first number corresponds to the mean value of the scaling factor and the second to the square of the standard deviation. The purpose of these calculations was to determine which “defect” content is sufficient to describe the patterns of shear bands observed in our experiments. The selected mean value of the scaling factor ensured that the results of numerical calculations were close to the experimentally observed patterns of shear bands. Figure 11 presents the results of these calculations.

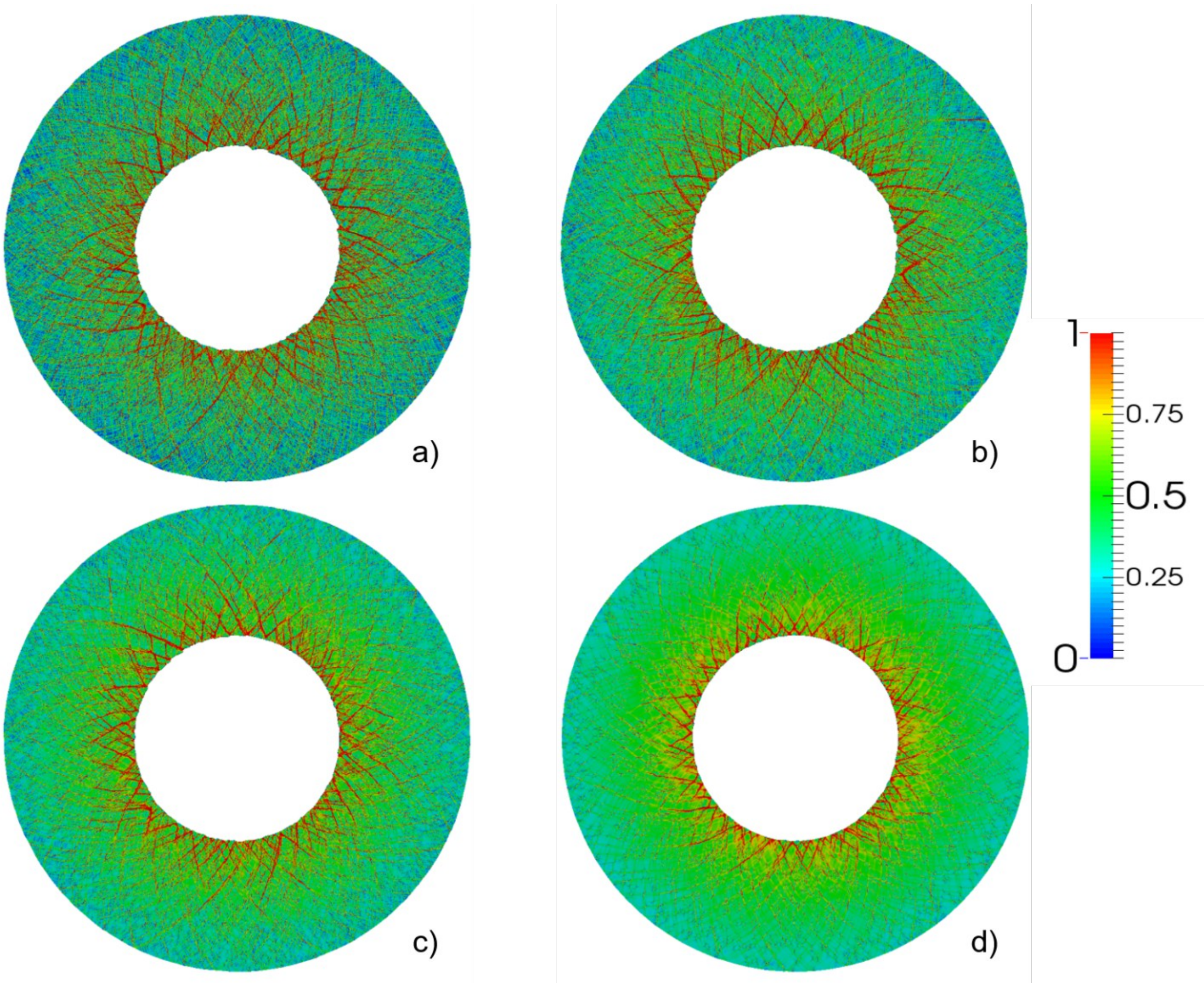


**Figure 11**. Fringe plots of effective plastic strain in the collapsed AISI 4340 samples with nominal properties in the majority of mesh elements and variable percentages (a) - 5%; (b) - 2.5%; (c) - 1.5%; and (d) - 0.5% of mesh elements with a different initial yield strength scaled by the nominal yield strength. Data correspond to large global strain (the test with 0.5-mm-wall copper stopper tube), outer diameter in all figures is 13.44 mm. “Defects” are randomly distributed through the specimen and follow a normal distribution $N(0.1, 0.0025)$.

From the presented results, it is clear that the number of “defects” introduced in the calculations directly related to the number of nucleated shear bands and the length of the evolved shear bands.

Figure 11(a), with 5% of mesh elements with “defects” shows a large number of shear bands that have evolved in the specimen in both clockwise and counter clockwise direction, which is contrary to what is observed in the experiments where a dominant direction is exhibited.

Similarly, with 2.5% and 1.5% of “defects” (Fig. 11(b) and 11(c)), one cannot observe a dominant direction of shear band propagation and the number of shear bands is obviously greater then was observed in experiments.

The case with 0.5% “defects” present shear bands with significantly smaller lengths than in previous cases shown in Fig. 11(a)-(c). In Fig. 11(d), the developed shear bands only go through about one third of the specimen and we can see much of the localization contained within this area. In the other cases, Fig. 11(a)-(c), we can see how shear bands propagate more than half way through the specimen or all the way to the outer surface. We consider that the case with 0.5% “defects” is the closest to the observed experimental behavior of AISI 4340 (Fig. 2(b))

It is important to emphasize that symmetrically-nucleated shear bands propagating in both directions at 45 ° to radius lose symmetry while they propagate, with some of the shear bands developing faster, , which in turn blocks shear band propagation normal to these.

We conduct numerical calculations at two different strain levels of collapsed samples by using different wall thickness of copper stopper tubes, 0.5 mm and 1mm. The results of these calculations are presented in Fig. 12. Copper is simulated defect-free (it is resistant to shear localization at these strains) while defects are introduced in 0.5% of the elements in AISI 4340 steel to initiate the localization process (Section 3.2).

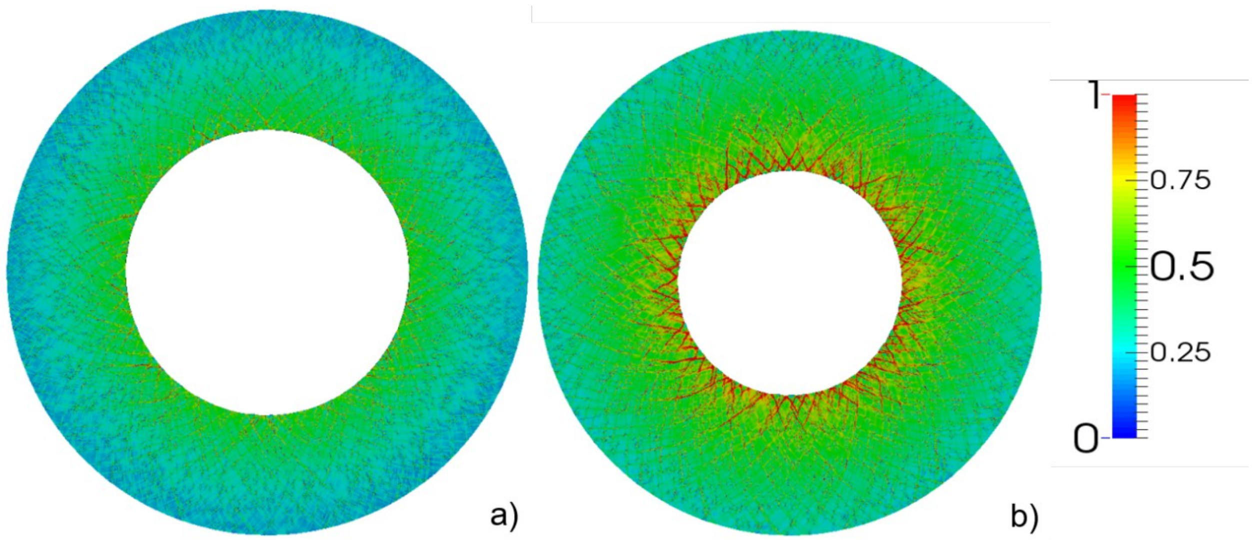


**Figure 12**. Fringe plot of the effective plastic strain in AISI 4340 Steel with (a) 1 mm and (b) 0.5 mm wall thickness of copper stopper tube corresponding to similar outer diameter of samples to experiments (see Table 2), percentage of elements with the scaled strength 0.5%. Outer diameter in (a) is 14.22 mm and in (b) 13.44 mm.

Figures 12(a) and 12(b) represent the results of numerical calculations that correspond to similar outer diameters to those observed in experiments (Table 2). These figures should be compared to the pattern of nucleated shear bands in the experiments shown in Fig. 2. In the case of 1 mm wall thickness copper stopper tube (Fig. 2(a) vs Fig. 12(a)), the final outer diameter of steel sample in the experiments (14.22 mm) corresponds to a final inner diameter of 7.75 mm in our calculations. The measured inner diameter results in an equivalent effective strain of 0.208; this effective strain is close to the effective strain found in experiments of 0.21. The distance between shear bands that can be identified in the specimen in the numerical calculations, denoted by red zones in Fig. 12(a), are in the range 1 - 1.1 mm.

For the case of 0.5 mm wall thickness of copper stopper tube (Fig. 2(b) vs. Fig. 12(b)), the final diameter in experiments is 13.44 mm (Table 2), which corresponds to the final inner diameter in calculations 5.991 mm. This inner diameter is related to an effective strain of 0.2744 compared to 0.27 from the experiments. In this case, the well-established shear bands (the ones that have reached a quarter of the specimen) are spaced about 0.75 mm apart. The decrease of spacing is due to the reduced radius of the inner surface of the sample and not related to the increase of the number of shear bands. In numerical calculations, we see that some shear bands are developing faster as we observe in experiments (Fig. 2(b)).

In these numerical calculations, no clear preferential direction of the bands has been observed. Shear bands nucleated in both counter and clockwise directions, but some of the shear bands stop growing once they interact with each other.

### *3.2 Shear localization and Post Critical Behavior of Heat Treated AISI 4340*

The patterns of shear bands in AISI 4340 and in the hardened AISI 4340 in the experiments were dramatically different at similar strain and strain rates. The heat treatment significantly changed the microstructure and steel properties. In our numerical calculations, we used experimentally identified material constants in the Johnson-Cook model for hardened AISI 4340 [53]. We retained percentage of defects equal 0.5%, which resulted in good agreement with the observed experimental behavior of AISI 4340 (Fig. 2(b)). This allowed us to minimize the number of variable initial properties of the samples, focusing instead on the role of material constants on the pattern of shear bands.

It is important to notice, that the damage constants D1-D5 (which determine the deletion of elements) were selected the same for both steels. In a separate set of numerical calculations we explored the case with the values of these constants being half, double and four times larger than used in this paper. It resulted in no significant changes of shear bands pattern, other than less or more accentuation of the shear bands. In the numerical model, these constants are used to estimate the damage on each element and to trigger their erosion (deletion), but this won't effectively cause major changes of the location of the bands. This reinforces the fact that the bands are mainly dictated by the initial number and location of defects.

Figure 13 show the fringe plot of the plastic strain for the case of small global strains (1 mm wall thickness of the copper stopper tube) at different times.

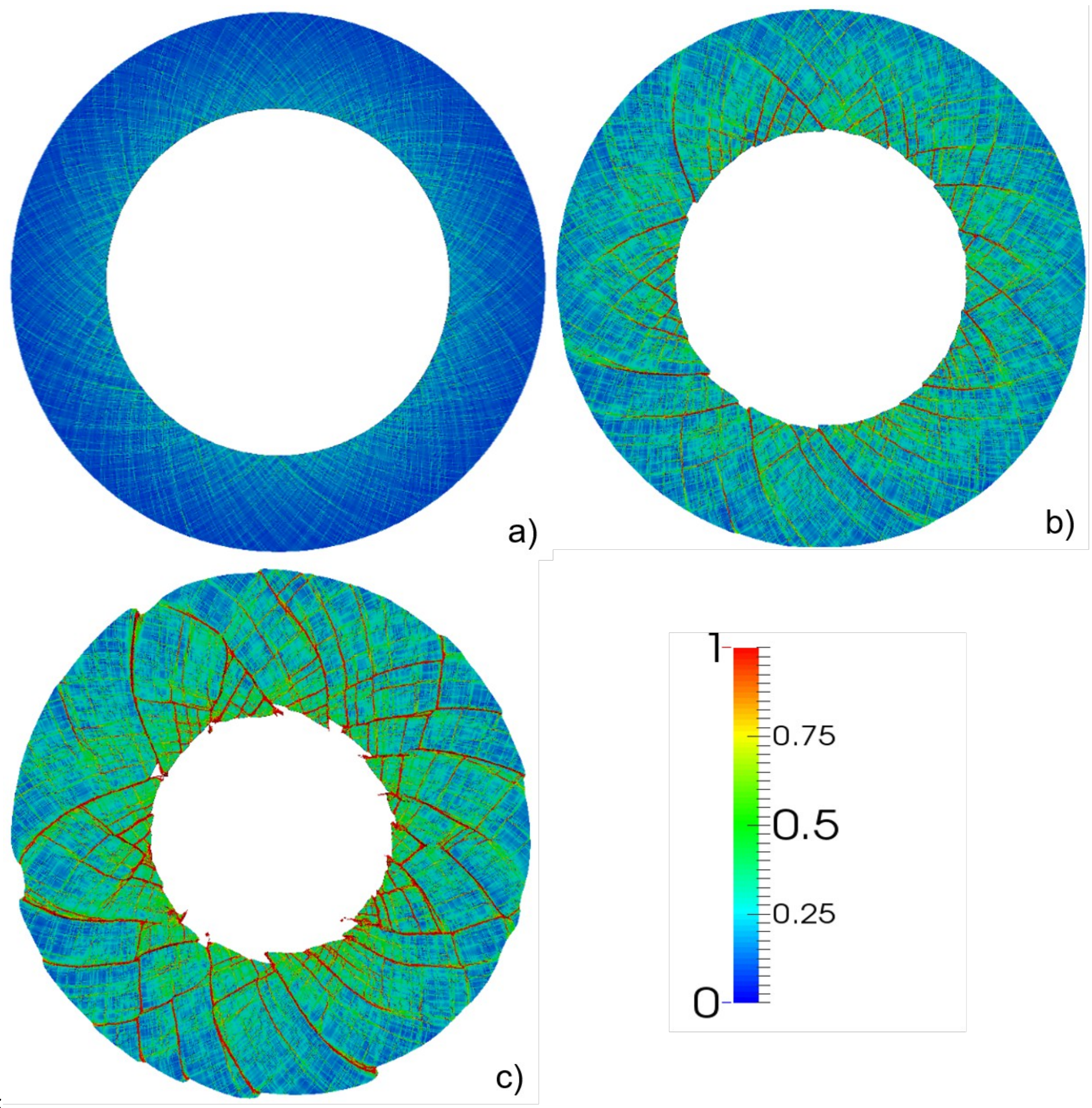

**Figure 13**. Fringe plot of the effective plastic strain on hardened 4340 Steel (percentage of defects 0.5%) with 1 mm wall copper stopper tube at different stages of collapse (a) 5 μs (b) 7.88 μs (same effective strain as Fig. 12(b)) (c) 10 μs. Outer diameters in (a) 15.71 mm, in (b) 14.22 mm and in (c) 13.28 mm.

It is clear from the comparison of Figs. 12 and 13, that changing material properties resulted in the dramatic change of shear band patterns in the numerical calculations (compare Fig. 12 (a) and Fig. 13 (b)) taken at the similar inner diameters of the samples.

We also observe that changes in the shear band pattern in the numerical calculations for hardened samples are similar to those observed in experiments (compare Fig. 13 and Fig. 4(a)). But in numerical calculations shear bands propagating through the whole sample have been formed more uniformly through the sample bulk in both directions compared to the ones observed in the experiment. The possible explanation can be a slight asymmetry of the collapse in experiments and fast growth of individual shear bands that arrest development of more symmetric shear band patterns that are observed in numerical calculations.

If we measure the spacing between bands considering the bands that have reached or almost reached the outer surface in Fig. 12(b) and Fig. 13(b), we obtain a spacing approximately equal to 1.1 mm. The main difference between AISI 4340 as-received vs. hardened specimen was observed in their post-critical behavior. The results of numerical calculations coincide with catastrophic failure observed in experiments (compare Fig. 13 and Fig. 4(a)). It should be mentioned that Figs. 13(c) and 14(c) correspond to the final stage of the simulation, the boundary conditions were imposed such that the complete collapse of the specimen would take about 10 μs.

Figure 14 presents the case of large global strain (0.5 mm wall thickness copper stopper), which corresponds to experimental results depicted in Fig. 4(b). The number and location of the initial defects introduced in the calculations are identical to the ones corresponding to the smaller global strain (Fig. 12(b)).

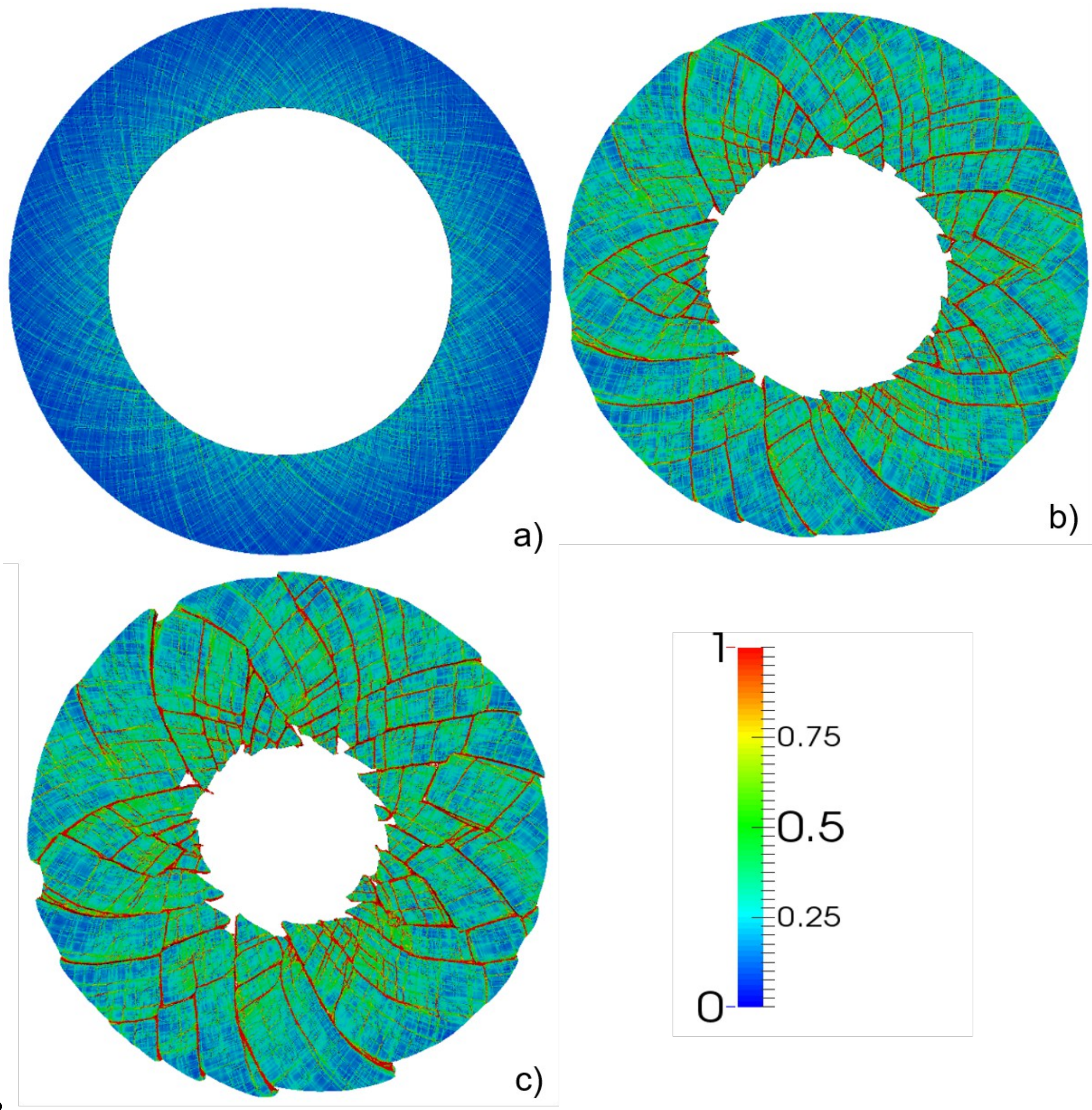


**Figure 14**. Fringe plot of the effective plastic strain on hardened 4340 Steel (0.5% defects) with 0.5 mm wall copper stopper tube at different times (a) 5 μs (b) 8.74 μs (same effective strain as Fig. 10(b)) (c) 10 μs.  Outer diameters in (a) 15.58 mm, in  (b) 13.44 mm and in (c) 12.7 mm.

As in the case of the small global strain, the number of observed shear bands is larger than observed in the experiments. The number of shear bands formed at earlier stages are similar to the number of shear bands in the later stages. Thus, initially created shear bands are able to accommodate the global shear strains without generation of additional shear bands (Fig. 13 vs. Fig. 14). This means that shear bands formed at small strains dominate the final stage of collapse and post-critical behavior similar to observed for other materials in [21]. At the same time, some shear bands in the numerical calculations propagated faster, arresting development of the neighboring shear bands and breaking a symmetric pattern on the earlier stages of collapse (Fig. 14 (b)). It is important to remark that even if shear bands resulted in fracture, no preferential direction of the shear bands can be observed.

In experiments (Fig. 4) and in numerical simulations (Figs. 13, 14), corresponding to the hardened 4340 steel, a secondary bands were observed on the post critical stage of sample deformation probably due to violent bending of dislodged material pieces between original shear bands. The fact that we observed it only in hardened 4340 is probably due to its lower ductility than in as received 4340 and in other investigated ductile materials e.g., in [13, 20-22]. The generation of additional damage due to bending on post critical stages of collapsing SiC cylinders with pattern of shear band was reported in paper [56].

## 4. – Conclusions

The role of the initial microstructure, resulting in different microhardness and ductility on shear band patterning in AISI 4340 steel in the plane strain geometry of the TWC method was investigated at practically identical conditions of dynamic deformation. It was observed that the initial hardening dramatically changes the nucleation and pattern of developed shear bands in the post-critical stage in AISI 4340 steel, mostly due to the change of material properties. The softening mechanism in both materials is probably caused by microcracking at interfaces of inclusions with the matrix. The hardening due to heat treatment of 4340 steel results in the dramatic difference in the pattern of shear bands because initial stage of their nucleation is sensitive to material properties. A well-developed pattern of shear bands results in the reduced ability to dissipate energy on post critical stages of high strain deformation due to low shear strength within them. Numerical modeling in the framework of the Johnson-Cook model with damage incorporating the random distribution of initial defects (by randomly scaling of initial yield strength in some elements) reproduced most qualitative features of the shear band patterning and its change with variation of the initial properties of materials. It is important that the material parameters of both steels were taken from independent experiments. The only fitting variable was the initial concentration of defects randomly distributed through the steel specimens modeled by mesh elements having a different initial yield strength scaled by the nominal yield strength.

The presented models verified in the experiments can be used to describe post-critical behavior of AISI 4340 steel with different initial microstructures at other dynamic conditions of loading, e.g., in target or penetrator deformation and fragmentation or in machining.

## 5. – Acknowledgments

The support of this project was provided by the Office of Naval research Multidisciplinary University Research Initiative Award N00014-07-1-0740, Program Manager Dr. Clifford D. Bedford. P.F.N. wants to thank CONACYT-UCMEXUS for the funding provided to make this work possible.

**6. – References**

[1] Dodd B, Bai Y. eds., Adiabatic shear localization: frontiers and advances. Elsevier; 2012.

[2] Wright TW. The physics and mathematics of adiabatic shear bands. Cambridge University Press; 2002.

[3] Miguélez MH, Soldani X, Molinari A. Analysis of adiabatic shear banding in orthogonal cutting of Ti alloy. International Journal of Mechanical Sciences 2013; 75: 212-222.

[4] Nesterenko VF. Dynamics of heterogeneous materials. Springer Science & Business Media; 2013. Chapter 4.

[5] Walley SM. Shear localization: a historical overview. Metallurgical and materials transactions A 2007; 38 (11): 2629-2654.

[6] Zener C, Hollomon J.H. Effect of strain rate upon plastic flow of steel. Journal of Applied physics 1944; 15(1): 22-32.

[7] Dodd B, Walley SM, Yang R, Nesterenko VF. Major steps in the discovery of adiabatic shear bands. Metallurgical and Materials Transactions A 2015; 46(10): 4454-4458.

[8] V.P. Kravz-Tarnavskii: A peculiar band discovered in steel, J. Russ. Metall. Soc., 1928; 3: 162-67, in Russian, (English translation of this paper can be found in Dodd B, Walley SM, Yang R, Nesterenko VF., Major steps in the discovery of adiabatic shear bands, http://arxiv.org/abs/1410.1353).

[9] Davidenkov N, Mirolubov I. Eine besondere art der stauchdeformation von stahl: Der krawz-tarnawskij effekt. Tech. Phys. USSR 1935; 2: 281-298, in German (English translation of this paper can be found in Dodd B, Walley SM, Yang R, Nesterenko VF. Major steps in the discovery of adiabatic shear bands, http://arxiv.org/abs/1410.1353).

[10] Nesterenko VF, Lazaridi AN, Pershin SA. Localization of deformation in copper by explosive compression of hollow cylinders. Fiz. Goreniya Vzryva 1989; 25(4): 154-155.

[11] Nesterenko VF, Bondar' MP. Localization of deformation in collapse of a thick walled cylinder. Combustion, Explosion, and Shock Waves 1994; 30(4): 500-509.

[12] Nesterenko VF, Bondar MP. Investigation of deformation localization by the “thick-walled cylinder” method. DYMAT Journal 1994; 1(3): 245-251.

[13] Xue Q, Nesterenko VF, and Meyers MA. Evaluation of the Collapsing Thick-Walled Cylinder Technique for Shear Band Spacing. Int J Impact Eng 2003; 28 (3): 257-280.

[14] Nesterenko VF, Meyers MA, Chen HC, LaSalvia JC. Controlled high-rate localized shear in porous reactive media. Applied physics letters 1994; 65(24): 3069-3071.

[15] Chiu PH, Olney KL, Higgins A, Serge M, Benson DJ, Nesterenko VF. The mechanism of instability and localized reaction in the explosively driven collapse of thick walled Ni-Al laminate cylinders. Applied Physics Letters 2013; 102(24): 241912.

[16] Olney KL., Chiu PH, Ribero Vairo MS, Higgins A, Serge M, Benson DJ, Nesterenko VF. Influence of mesoscale properties on the mechanisms of plastic strain accommodation in plane strain dynamic deformation of concentric Ni-Al laminates. Journal of Applied Physics 2015; 117(4): 044302.

[17] Yang Y, Zheng HG, Shi ZJ, Zhang QM. Effect of orientation on self-organization of shear bands in 7075 aluminum alloy. Materials Science and Engineering A 2011; 528(6): 2446-2453.

[18] Yang Y, Zheng HG, Zhao ZD, Zhang Q, Zhang, QM, Jiang F, Li XM. Effect of phase composition on self-organization of shear bands in Ti-1300 titanium alloy. Materials Science and Engineering A 2011; 528(25): 7506-7513.

[19] Stokes JL, Nesterenko VF, Shlachter JS, Fulton RD, Indrakanti SS, Ya Bei Gu. Comparative behavior of Ti and Stainless Steel in a Magnetically-Driven Implosion at the Pegasus-II Facility, Proceedings of International Conference on Fundamental Issues and Applications of Shock-Wave and High-Strain-Rate Phenomena, Edited by K.P. Staudhammer, L.E. Murr, and M.A. Meyers, 2001, Elsevier, Amsterdam: 585-592.

[20] Lovinger Z, Rikanati A, Rosenberg Z, Rittel D. Electro-magnetic collapse of thick-walled cylinders to investigate spontaneous shear localization. International Journal of Impact Engineering 2011; 38: 918-929.

[21] Lovinger Z, Rittel D, Rosenberg Z. An experimental study on spontaneous adiabatic shear band formation in electro-magnetically collapsing cylinders. Journal of the Mechanics and Physics of Solids 2015; 79: 134-156.

[22] Lovinger Z, Rittel D, Rosenberg Z. Modeling spontaneous adiabatic shear band formation in electro-magnetically collapsing thick-walled cylinders. Mechanics of Materials 2017; (in press).

[23] Dong XL, Li LZ, Fu YQ, Zhou FH. A FEM Study on Adiabatic Shear Band Formation in Tube Compression Driven by Electro-Magnetic Loading. Applied Mechanics and Materials 2014; 566: 517-521.

[24] Cai J, Nesterenko VF. Collapse of Hollow Cylinders of PTFE and its Mixtures with Metal Particles Using Hopkinson Bar, in SHOCK COMPRESSION OF CONDENSED MATTER

2005, Proceedings of the Conference of the American Physical Society Topical Group on Shock Compression of Condensed Matter, AIP Conference Proceedings 845, edited by M.D. Furnish, M. Elert, T.P. Russel, and C.T. White, American Institute of Physics, Melville, New York, pp. 793-796, 2006.

[25] Winter RE, Stirk SM, Harris EJ, Chapman DJ, Eakins DE. A technique for studying the response of materials to high rate, high strain deformation. International Journal of Impact Engineering 2016; 97: 116-126.

[26] Grady DE, Kipp ME. The growth of unstable thermoplastic shear with application to steady-wave shock compression in solids. Journal of the Mechanics and Physics of Solids 1987; 35(1): 95-119.

[27] Grady D.E, Asay JR, Rohde RW, Wise JL. Microstructure and mechanical properties of precipitation hardened aluminum under high rate deformation. In Material Behavior Under High Stress and Ultrahigh Loading Rates 1983; 81-100, Springer US.

[28] Wright TW, Ockendon H. A scaling law for the effect of inertia on the formation of adiabatic shear bands. International journal of plasticity 1996; 12(7): 927-934.

[29] Molinari A. Collective behavior and spacing of adiabatic shear bands. Journal of the Mechanics and Physics of Solids 1997; 45(9): 1551-1575.

[30] Mingtao Liu, Zhaoliang Guo, Cheng Fan, Tiegang Tang, Xiaoyan Wang, Haibo Hu. Modeling spontaneous shear bands evolution in thick-walled cylinders subjected to external High-strain-rate loading. International Journal of Solids and Structures 2016; 97: 336–354.

[31] Rabczuk T, Areias P.M.A, Belytschko T. A simplified mesh-free method for shear bands with cohesive surfaces. International Journal for Numerical Methods in Engineering 2007; 69(5): 993-1021.

[32] Zhou F, Wright TW, Ramesh KT. A numerical methodology for investigating the formation of adiabatic shear bands. Journal of the Mechanics and Physics of Solids 2006; 54(5); 904-926.

[33] Zhou F, Wright TW, and Ramesh KT. The formation of multiple adiabatic shear bands. Journal of the Mechanics and Physics of Solids 2006; 54(7): 1376-1400.

[34] Tan ZH, Han X, Zhang W, Luo SH. An investigation on failure mechanisms of ceramic/metal armour subjected to the impact of tungsten projectile. International Journal of Impact Engineering 2010; 37(12): 1162-1169.

[35] Frew DJ, Hanchak SJ, Green ML, Forrestal MJ. Penetration of concrete targets with ogive-nose steel rods. International Journal of Impact Engineering 1998; 21(6): 489-497.

[36] Littlefield DL, Anderson CE, Partom Y, Bless SJ. The penetration of steel targets finite in radial extent. International journal of impact engineering 1997; 19(1): 49-62.

[37] Schroeder T, Hazra J, Von Turkovich BF, FIom DG. On the catastrophic shear instability in high-speed machining of an AISI 4340 steel. Journal of Engineering for Industry 1982; 104: 121-131.

[38] Hou ZB, Komanduri R. Modeling of thermomechanical shear instability in machining. International Journal of Mechanical Sciences 1997; 39(11): 1273  1314.

[39] Guo YB, Yen DW. A FEM study on mechanisms of discontinuous chip formation in hard machining. Journal of Materials Processing Technology 2004; 155: 1350-1356.

[40] Lee WS, Yeh GW. The plastic deformation behaviour of AISI 4340 alloy steel subjected to high temperature and high strain rate loading conditions. Journal of materials processing technology 1997; 71(2): 224-234.

[41] Wittman CL, Meyers MA, Pak HR. Observation of an adiabatic shear band in AISI 4340 steel by high-voltage transmission electron microscopy. Metallurgical transactions A 1990; 21(2): 707-716.

[42] Mason C, Worswick MJ. Adiabatic shear in annealed and shock-hardened iron and in quenched and tempered 4340 steel. International journal of fracture 2001; 111(1): 29-51.

[43] Odeshi AG, Bassim MN, Al-Ameeri S, Li Q. Dynamic shear band propagation and failure in AISI 4340 steel. Journal of materials processing technology 2005; 169(2): 150-155.

[44] Owolabi G, Odoh D, Odeshi A, Whitworth H. Occurrence of dynamic shear bands in AISI 4340 steel under impact loads. World Journal of Mechanics 2013; 3: 139-145.

[45] Lee WS, Yeh GW. The plastic deformation behavior of AISI 4340 alloy steel subjected to high temperature and high strain rate loading conditions. Journal of materials processing technology 1997; 71(2): 224-234.

[46] Yiadom SB, Khan AK, Bassim N Effect of microstructure on the nucleation and initiation of adiabatic shear bands (ASBs) during impact. Materials Science and Engineering A 2014; 615: 373-394.

[47] Washko SD, Aggen G. Wrought stainless steels. ASM International, Metals Handbook. Tenth Edition., 1990; 1: 841-907.

[48] Zurek AK. The study of adiabatic shear band instability in a pearlitic 4340 steel using a dynamic punch test, Metallurgical and Materials Transactions A 1994; 25: 2483-2489.

[49] Meyers MA, Wittman CL. Effect of metallurgical parameters on shear band formation in low-carbon (∼0.20 Wt Pct) steels, Metall. Trans. A 1990; 21: 3153-3164.

[50] Antolovich SD, Armstrong RW. Plastic strain localization in metals: origins and Consequences. Progress in Materials Science 2014; 59: 1–160.

[51] Cox TB, Low Jr JR. An investigation of the plastic fracture of AISI 4340 and 18 Nickel–200 grade maraging steels. Metal. Trans 1974; 5: 1457–1470.

[52] Bassim MN, Odeshi AG. Shear strain localization and fracture in high strength structural materials. Archives of Materials Science 2008; 70: 69-74.

[53] Barry J, Byrne G. TEM study on the surface white layer in two turned hardened steels. Materials Science and Engineering a-Structural Materials Properties Microstructure and Processing 2002; 325(1-2): 356-364.

[54] Johnson GR, Cook WH. Fracture characteristics of three metals subjected to various strains, strain rates, temperatures and pressures. Engineering fracture mechanics 1985; 21(1): 31-48.

[55] Gray GT, Chen SR, Wright W, Lopez MF. Constitutive equations for annealed metals under compression at high strain rates and high temperatures. Los Alamos National Laboratory 1994, LA-12669-MS, Los Alamos.

[56] Shih CJ, Nesterenko VF, Meyers MA. High-Strain-Rate Deformation and Comminution of Silicon Carbide. J. Appl. Phys. 1998; 83(9): 4660 – 4671.